

Predict open quantum dynamics with data-informed quantum-classical dynamics

Pinchen Xie,^{1,*} Ke Wang,² Anupam Mitra,¹ Yuanran Zhu,¹ Xiantao Li,² Wibe Albert de Jong,¹ and Chao Yang^{1,†}

¹*Applied Mathematics and Computational Research Division,
Lawrence Berkeley National Laboratory, Berkeley, CA 94720, USA*

²*Department of Mathematics, Pennsylvania State University, University Park, PA 16802, USA*
(Dated: August 26, 2025)

We introduce a data-informed quantum-classical dynamics (DIQCD) approach for predicting the evolution of an open quantum system. The equation of motion in DIQCD is a Lindblad equation with a flexible, time-dependent Hamiltonian that can be optimized to fit sparse and noisy data from local observations of an extensive open quantum system. We demonstrate the accuracy and efficiency of DIQCD for both experimental and simulated quantum devices. We show that DIQCD can predict entanglement dynamics of ultracold molecules (Calcium Fluoride) in optical tweezer arrays. DIQCD also successfully predicts carrier mobility in organic semiconductors (Rubrene) with accuracy comparable to nearly exact numerical methods.

Despite the inevitable coupling between quantum devices and noisy environments containing vast degrees of freedom, device performance can be characterized based on the statistical and dynamical behaviors of a few observables. Dynamical modeling can focus on a subsystem of the device-environment duo, treating the rest of the system as an effective bath that perturbs the subsystem in a way that yields similar statistics and dynamics of observables relevant to device metrics. Such dimension-reduction ideas evolve into a sequence of numerical approaches for modeling equations of motion (EOM) governing open quantum system dynamics, with a tradeoff between accuracy and efficiency [1–11].

For example, on the high-accuracy end, pseudomode methods [5, 10, 12–14] enlarge the system Hilbert space to incorporate a finite set of effective modes that encode the correlation function of a Gaussian bath. On the high-efficiency end, the plain Lindblad equation sketches a dissipative environment without introducing auxiliary degrees of freedom, similar to how the Langevin equation sketches a classical environment. In between, mixed quantum-classical dynamics (MQCD) may strike the balance of accuracy and efficiency. With additional classical degrees of freedom, MQCD can describe coherent fluctuations in quantum evolution, which is otherwise reduced to mean-field dissipators in the plain Lindblad equation.

Well-known phenomenological MQCD approaches such as Ehrenfest dynamics [15] and surface hopping [16] have been intensively used for modeling non-adiabatic molecular dynamics. There are concerns about unsystematic control of error regarding the exact quantum dynamics [17]. Uncontrolled error hinders accurate predictions of material properties or device metrics. Moreover, for systems where the environment does not have a particle-based semiclassical representation, phenomenological MQCD becomes irrelevant. For example, one needs to devise special-purpose, *ab initio* quantum-classical models for cold-atom systems [18].

In this work, we place phenomenological MQCD within a general context by introducing variational capacity on

the classical dynamics and the quantum-classical coupling. The variational capacity can be understood as a mechanism to renormalize MQCD, thereby circumventing the limited applicability of non-variational MQCD approaches. We develop the algorithm and the software for optimizing a general MQCD EOM, parameterized as a time-dependent Lindblad equation, on time series data of measurements on observables relevant to device metrics. We call our method Data-Informed Quantum-Classical Dynamics (DIQCD). The approach emphasizes practicality for dealing with experimental or simulation time-series data. DIQCD requires only the data that represents measurements performed on the quantum subsystem of interest, without requiring the time-correlation function of the quantum environment. DIQCD works well with sparse and noisy data due to its restricted variational flexibility, which reduces generality but avoids overfitting. These features allow the application of DIQCD to various real-world challenges.

We will demonstrate the applications of DIQCD for both artificial quantum systems and condensed matter systems, with data from either experiments or first-principles-based simulations. The first case study is on controlled dynamics of Calcium-fluoride (CaF) molecular qubits in optical traps [19]. We train DIQCD-EOM on sparse experimental data collected from a single CaF molecule. We show that DIQCD can capture quantum decoherence across multiple time scales and predict two-qubit dynamics of Bell state generation. The second case study is on quantum transport in Rubrene crystal ($\text{C}_{18}\text{H}_8(\text{C}_6\text{H}_5)_4$). We train DIQCD-EOM on simulation data collected for a single Rubrene molecule. With the cost of simulating a tight-binding model, DIQCD predicts carrier mobility with similar accuracy as nearly exact time-dependent density matrix renormalization group (TD-DMRG) simulation [20] of the whole system (carrier and phonons). The study brings a new perspective for overcoming the accuracy-efficiency tradeoff in modeling band-like transport.

Methods – In the following, we call the quantum sub-

system of interest the “system”, and the rest of the degrees of freedom the “environment”. The DIQCD approach is made up of a flexible EOM for describing system evolution, a loss function for optimizing the EOM on data, and the corresponding training and simulation algorithms. The EOM in DIQCD is a Lindblad equation with a time-dependent Hamiltonian $\hat{H}_\epsilon(t)$:

$$\frac{d\hat{\rho}_\epsilon(t)}{dt} = -i[\hat{H}_\epsilon(t), \hat{\rho}_\epsilon(t)] + \sum_k \gamma_k (\hat{L}_k \hat{\rho}_\epsilon(t) \hat{L}_k^\dagger - \frac{1}{2} \{ \hat{L}_k \hat{L}_k^\dagger, \hat{\rho}_\epsilon(t) \}). \quad (1)$$

$\hat{\rho}_\epsilon(t)$ is the density matrix of the system. $\{\hat{L}_k\}$ is a finite set of static jump operators. $\hat{H}_\epsilon(t) = \hat{H}_0 + \hat{H}_c(t) + \sum_{j=1}^M f_j(\epsilon(t)) \hat{S}_j$ combines the static system Hamiltonian \hat{H}_0 , the external control $\hat{H}_c(t)$, and perturbing Hermitian operators \hat{S}_j . $f_j(\epsilon(t))$ is a scalar function of the multidimensional, classical dynamical processes $\epsilon(t)$ that encodes information about the environment. As a special case, Eq. (1) becomes Ehrenfest dynamics when $\epsilon(t)$ represents atomic nuclei evolving under the average potential energy surface $\text{Tr}(\hat{H}_\epsilon(t) \rho_\epsilon)$. In DIQCD, we allow $\epsilon(t)$ to be generic dynamical processes that can be integrated by an explicit Markovian integrator with or without auxiliary degrees of freedom $\xi(t)$. This means $\epsilon(t + \delta t)$ and $\xi(t + \delta t)$ are determined by $\epsilon(t)$ and $\xi(t)$ in an integration scheme with δt as the time step. These requirements are imposed such that $\epsilon(t)$ can evolve concurrently with the structure-preserving integration [21] of the Lindblad equation. And eventually, the parameters controlling the EOM of $\epsilon(t)$ can be optimized together with other system parameters (such as γ_k) through chain rules, such that the behavior of $\hat{\rho}_\epsilon(t)$ can match time-series data of the system. A Langevin process $\epsilon_0(t)$ is an example of a flexible classical process. The EOM of $\epsilon_0(t)$ is parameterized by τ and A with the scheme [22] $\epsilon_0(t + \delta t) = e^{-\delta t/\tau} \epsilon_0(t) + A\sqrt{1 - e^{-2\delta t/\tau}} \xi_0(t)$. $\xi_0(t)$ is randomly sampled from a standard normal distribution. Simpler examples of flexible processes include periodic signals and Gaussian white noise. Complex examples include isothermal molecular dynamics on a parameterized potential energy surface.

In DIQCD, the expectation of any system observable \hat{O} at time t is given as $O(t) = \langle O_\epsilon(t) \rangle_\epsilon = \langle \text{Tr}(\hat{O} \hat{\rho}_\epsilon(t)) \rangle_\epsilon$, where $\langle \cdot \rangle_\epsilon$ represents the average over realizations of $\epsilon(t)$ with given probability distribution of $\epsilon(0)$ and possible auxiliary variables $\xi(0)$. DIQCD is trained on time-series data at discrete time points $\{t_1, t_2, \dots\}$ with the mean-squared loss $\mathcal{L} = \sum_{ij} (O_i(t_j) - O_i^*(t_j))^2$. The data $O_i^*(t)$ comes from measurements performed on either an experimental or simulated system. For example, for an atom-based quantum computing platform, \hat{O}_i can be a Pauli operator acting on the i -th qubit, and $\epsilon(t)$ conceptually embeds dynamical information about optical traps, environmental radiation, etc. In DIQCD, one does not need to model $\epsilon(t)$ with an accurate understanding of possible system-environment interaction. Various classical

processes can be incorporated. A guiding principle for practical modeling is to choose a set of processes with flexible time scales [23] initialized to roughly cover the orders of magnitude of time scales from δt to quantum coherence time, and also infinity (shot-by-shot noise). Other than that, DIQCD does not guide the choice of $\{\hat{S}_j\}$ or the choice of system degrees of freedom. These considerations should be made with a phenomenological understanding of a quantum device.

Details on the implementation of DIQCD, i.e., the GPU-enabled Python package QEpsilon [24], are reported in Appendix. In summary, QEpsilon provides a library of operators for constructing a many-body open quantum system, a library of classical processes, numerical integrators for classical and quantum processes, and a user interface for model construction, training, and simulation. The training is carried out as a forward-backpropagation loop: we simulate the forward evolution of $\rho_\epsilon(t)$ and $\epsilon(t)$ from time 0 to T , with plain numerical integration of Eq. (1) and relevant classical EOMs. We calculate the loss function \mathcal{L} , backpropagate the loss over the entire trajectory of $\rho_\epsilon(t)$ and $\epsilon(t)$, and update all flexible parameters with accumulated gradients.

CaF molecular qubits – Reconfigurable optical tweezer arrays of ultracold molecules have emerged as a promising platform for precision measurement and quantum simulation [25]. Realization of coherent molecular qubits [26] and generation of on-demand entanglement [19, 27] have recently been demonstrated. It is essential to model and characterize the limitations of these systems to improve their performance and unlock future possibilities. Here, we consider two CaF molecules in respective optical tweezers (see Fig. 1(b) for illustration and Appendix for technical details) separated by a center-to-center distance of d .

The trapping potential of single and double tweezers is illustrated in Fig. 1. Let $\mathbf{R}(t) = (\mathbf{r}_1(t), \mathbf{r}_2(t))$ be the center-of-mass positions of the two molecules. The quantum system here is relevant to two hyperfine states $|\uparrow\rangle$ and $|\downarrow\rangle$ of each molecule. Let $\hat{S}_i^\alpha = \frac{\hbar}{2} \hat{\sigma}_i^\alpha$ ($i = 1, 2$; $\alpha = x, y, z$) be spin-1/2 operator for molecule- i . A phenomenological Hamiltonian $H_\epsilon(t)$ for the system consists of the one-body terms $H_\epsilon^{(1)}(t) = \sum_{j=1}^L \epsilon_{1,j}(t) \hat{S}_1^z + \sum_{j=1}^L \epsilon_{2,j}(t) \hat{S}_2^z$, and the two-body dipole-dipole interaction $H_\epsilon^{(2)}(t) = J(\mathbf{r}_1, \mathbf{r}_2) (\hat{S}_1^x \hat{S}_2^x + \hat{S}_1^y \hat{S}_2^y)$. Here, $J(\mathbf{r}_1, \mathbf{r}_2) = \frac{J_0}{r_{12}^3} (1 - 3 \cos^2 \theta')$ with J_0 being the coupling constant, r_{12} being $\|\mathbf{r}_1 - \mathbf{r}_2\|$, θ' being the angle between $(\mathbf{r}_1 - \mathbf{r}_2)$ and the quantization axis (y -axis). For the experimental molecular temperature [19] without further cooling [28], quantum fluctuation in \mathbf{r}_1 and \mathbf{r}_2 is insignificant. So all relevant classical processes here are $\epsilon(t) = \{\epsilon_{1,j}(t)\} \cup \{\epsilon_{2,j}(t)\} \cup \{\mathbf{r}_1(t), \mathbf{r}_2(t)\}$. From phenomenological and experimental understanding of the environments, we take an ansatz with $L = 6$: $\epsilon_{i,l}$ ($l = 1, 2, 3, 4$) are periodic processes with fixed frequency $\omega_l = l \times 60\text{Hz}$ and flexible [29]

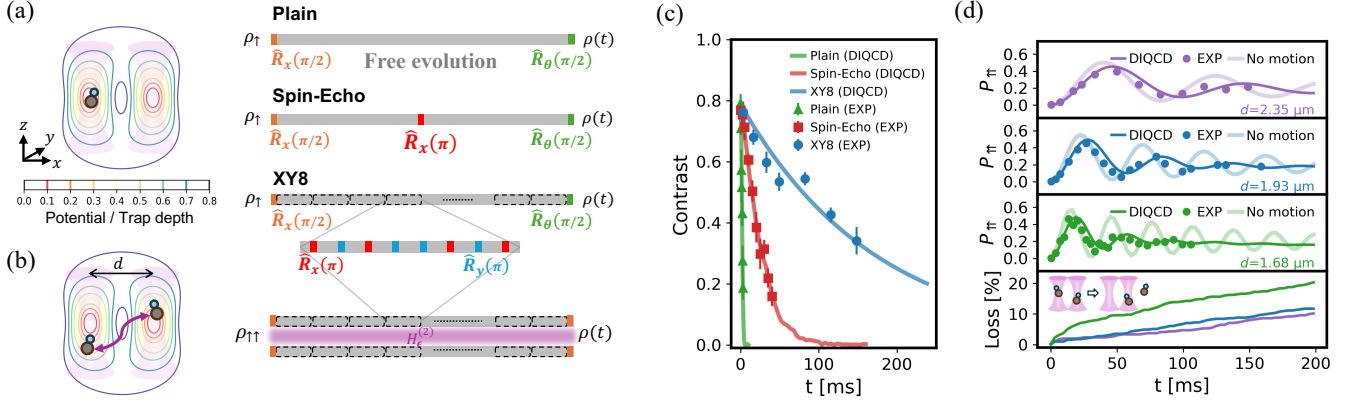


FIG. 1. (a) Optically trapped CaF molecule and three control schemes used in Ramsey experiments. Contour lines represent the equipotential surface of the trap, with energy levels indicated in the color map. (b) CaF molecules trapped in two optical tweezers and the control scheme for Bell state generation. (c) The contrast $C(t)$ (scaled by ζ) as a function of circuit duration t . Circle, square, and triangle markers represent $C^{\text{EXP}}(t)$ data. (d) The top three panels show $P_{\uparrow\uparrow}$ (scaled by ζ^2) as a function of t . The bottom panel shows the rate of qubit loss as a function of t .

amplitudes. $\epsilon_{i,5}$ are flexible, overdamped Langevin processes. $\epsilon_{i,6}$ are time-independent noises with uniformly distributed initial values sampled from a flexible interval. Here, $\epsilon_{i,l}$ ($l = 1, 2, 3, 4$) represent line noises from power sources. $\epsilon_{i,6}$ represents noises with a time scale above ms. The Langevin process $\epsilon_{i,5}$ with a continuous spectrum approximates the mix of other sources of noise with time scales comparable to execution time. The choices of these processes are not unique, but should be organized in a way that adaptively covers a large range of time scales encompassing the time scale of system dynamics.

The system EOM is then given by Eq. (1) with one-body jump operators $\{\hat{S}_i^x, \hat{S}_i^z\}_{i=1,2}$ and two flexible damping rates γ_x and γ_z , as a minimal parameterization of one-body dissipation. The EOM of $(\mathbf{r}_1, \mathbf{r}_2)$ is standard isothermal molecular dynamics without non-adiabatic force, because $\text{Tr}(\rho H_\epsilon^{(2)})$ is negligible for the all values of d used in experiments.

We train the DIQCD model on data from a series of one-molecule Ramsey experiments [19], where the motion of the molecule's position is irrelevant. Experiments were performed with initial state $|\uparrow\rangle$ and three external control schemes as illustrated in Fig. 1(a): a plain scheme, a spin-echo scheme, and an XY8 scheme. Because all external controls are short pulses, we do not include them as a continuous control $\hat{H}_c(t)$ in the Hamiltonian. Instead, they are modeled as instantaneous one-body unitary rotations $\hat{U} = \hat{R}_{\hat{n}}(\cdot)$ along axis \hat{n} , followed by a flexible error channel to account for instantaneous coherence loss. The combined effect (on the density operator) of the unitary rotation and the error channel is given as $\rho(t + \delta t) = \sum_{\alpha=1}^4 \hat{K}_\alpha \hat{U} \rho(t) \hat{U}^\dagger \hat{K}_\alpha^\dagger$. The Kraus operators ($\hat{K}_0 = \sqrt{1-p} \hat{I}$, $\hat{K}_1 = \sqrt{\frac{p}{3}} \hat{\sigma}_x$, $\hat{K}_2 = \sqrt{\frac{p}{3}} \hat{\sigma}_y$, $\hat{K}_3 = \sqrt{\frac{p}{3}} \hat{\sigma}_z$) are controlled by a flexible scalar p . The collected data from the Ramsey experiments is the spin-

up probability $P_{\uparrow}(t, \theta)$ as a function of circuit duration t and the angle θ associated with the last control pulse (see Fig. 1(a)). Let $C(t) = |P_{\uparrow}(t, \pi) - P_{\uparrow}(t, 0)|$. Experiments yield twenty-four $C^{\text{EXP}}(t)$ data points shown in Fig. 1(c), with a state preparation fidelity $\zeta \approx 0.79$. The undetermined parameters in $\{\epsilon_{1,j}\} \cup \{\epsilon_{2,j}\} \cup \{\gamma_x, \gamma_z, p\}$ are then optimized such that the $C(t)$ predicted by a single DIQCD model, but with three control schemes, will match all $C^{\text{EXP}}(t)/\zeta$ data. The solid lines in Fig. 1(c) are $\zeta C(t)$ from the optimized DIQCD, showing excellent agreement with experiments. The results imply that DIQCD captures the sources of decoherence over multiple time scales. The success would not be achieved by the plain Lindblad equation with mean-field dissipators. Also, the optimized DIQCD may be used to predict circuit outcome for other control schemes.

Next, we generalize the one-molecule DIQCD model to the two-molecule system by including the thermal dynamics of $\mathbf{R}(t)$ and the dipole-dipole interaction $H_\epsilon^{(2)}(t)$ in DIQCD. Radial (x and y directions) and axial (z direction) temperature of the molecules are set to $T_r = 6\mu\text{K}$ and $T_a = 18\mu\text{K}$ (from Raman Thermometry [28], see Appendix for details) for isothermal simulation of $\mathbf{R}(t)$. The resultant DIQCD model is not trained on any two-molecule experimental data. We will validate its prediction against experimental results on Bell state creation (See Fig. 1(b) and Appendix). The ideal (without decoherence or molecular motion) probability of observing $|\uparrow\uparrow\rangle$ from final measurement is $P_{\uparrow\uparrow} = \sin^2(\frac{J_0 t}{4\hbar d^3})$. The oscillation in $P_{\uparrow\uparrow}$ is damped in experimental measurements $P_{\uparrow\uparrow}^{\text{EXP}}$, plotted in Fig. 1(d) for different tweezer separation d . DIQCD can predict $\zeta^2 P_{\uparrow\uparrow}$ (solid lines in top three panels of Fig. 1(d)) in excellent consistency with $P_{\uparrow\uparrow}^{\text{EXP}}$. Moreover, molecular dynamics in the non-harmonic trap potential of optical tweezers predicts the rate of qubit

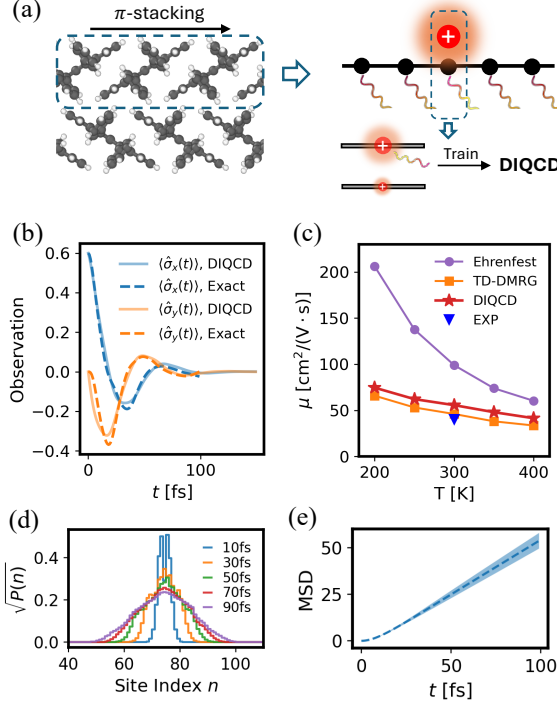


FIG. 2. (a) Orthorhombic Rubrene crystal (left panel), the effective model for describing carrier transport (upper right panel), and the effective model for a single Rubrene molecule (lower right panel). (b) Comparison of data and DIQCD on average $\langle \hat{\sigma}_x(t) \rangle$ and $\langle \hat{\sigma}_y(t) \rangle$ for $T = 300\text{K}$. (c) Carrier mobility as a function of temperature. The blue triangle is an experimental estimation of the intrinsic mobility of Rubrene [32]. (d) The square root of site occupation on the $L = 150$ molecular lattice. Snapshots are obtained from a DIQCD simulation lasting 100fs for $T = 300\text{K}$. (e) The mean squared displacement ($\text{MSD} = \langle \text{Tr}(\rho_\epsilon(t)n^2) - \text{Tr}^2(\rho_\epsilon(t)n) \rangle_\epsilon$) as a function of time for $T = 300\text{K}$. The shades represent standard deviation.

loss[30] due to molecules hopping from one optical trap to another. The qubit loss is plotted as a function of time in the bottom panel of Fig.1(d). The importance of modeling molecular dynamics is revealed when we simulate the DIQCD model with static CaF molecules fixed to tweezer centers — the resultant $\zeta^2 P_{\uparrow\uparrow}$ (semi-transparent lines in Fig.1(d)) shows underestimated damping and overestimated frequency of oscillation.

One can generalize the DIQCD model to a larger array of tweezers with pairwise dipolar interactions. DIQCD can also model molecules cooled to almost the motional ground state by replacing classical molecular dynamics with ring-polymer path-integral molecular dynamics [31].

Rubrene Crystal – The development of flexible electronics requires screening of high-mobility organic semiconductors [33]. Here we show the relevance of DIQCD with first principles-based prediction of the intrinsic carrier mobility of Rubrene crystal, an organic semiconductor with an exceptional room-temperature hole mobility $\mu \in [10, 40]\text{cm}^2/(\text{V} \cdot \text{s})$ [32, 34]. The high mo-

bility is due to the coherent quantum transport dominantly along the π -stacking direction. The effective model for transport in Rubrene crystal can therefore be reduced to a 1D Holstein model with the Hamiltonian $\hat{H} = \hat{H}_e + \hat{H}_{\text{ph}} + \hat{H}_{\text{e-ph}}$. Let n be the label of a Rubrene molecule on the 1D molecular lattice along the stacking direction. Let $\hbar = 1$. The single-carrier tight-binding Hamiltonian $\hat{H}_e = V \sum_n (c_{n+1}^\dagger c_n + c_n^\dagger c_{n+1})$ describes intermolecular carrier hopping. The harmonic Hamiltonian $\hat{H}_p = \sum_{n,m} \omega_m b_{n,m}^\dagger b_{n,m}$ is associated with the bosonic vibrational modes of each molecule. The interaction $\hat{H}_{\text{ep}} = \sum_{n,m} g_m \omega_m (b_{n,m}^\dagger + b_{n,m}) c_n^\dagger c_n$ is associated with electron-phonon coupling, of which the strength is characterized by the polaron binding energy $\lambda = \sum_m g_m^2 \omega_m$. It is challenging to model quantum transport when λ is on the same order of magnitude as V [35], which entails the inaccuracy of Marcus theory and the need to explicitly consider the dynamics of bosonic modes. Traditional phenomenological MQCD approaches can give a semi-quantitative description of the quantum transport, however with uncontrolled error. In contrast, advanced GPU-based TD-DMRG can simulate unitary dynamics driven by \hat{H} with nearly exact accuracy. TD-DMRG is restricted to a small length scale, corresponding to a few lattice sites, which allows the determination of μ with the Kubo formula, but not real-time, mesoscale transport dynamics [36].

In the following, we treat the carrier as the system, and all bosonic modes as the environment. We will demonstrate that DIQCD can achieve similar accuracy as TD-DMRG in describing carrier transport, with scalability and numerical efficiency comparable to simulating a tight-binding model. And such success requires only training data collected from simulating the unitary dynamics of one Rubrene molecule and its bosonic modes, since the main mechanism slowing down the coherent transport considered here is phase decoherence caused by local system-environment interaction.

We adopt the model of \hat{H} with $V = 83\text{meV}$, $\lambda = 73\text{meV}$, and nine renormalized vibration modes for each molecule with $g_m \in [0, 1]$, and $\omega_m \in [84, 1594]\text{cm}^{-1}$ (see Appendix for details). These parameters were obtained in Ref. [20, 37] from a hybrid-level density functional theory [38–40]. Here, we are mainly interested in deriving μ for temperatures near the room temperature. For $T \in \{200\text{K}, 250\text{K}, 300\text{K}, 350\text{K}, 400\text{K}\}$, we generate one-molecule data by simulating the plain unitary evolution driven by an effective spin-boson Hamiltonian $\hat{H}^{\text{eff}} = \sum_{m=1}^9 \omega_m b_m^\dagger b_m + \sum_{m=1}^9 \frac{1}{2} g_m \omega_m (b_m^\dagger + b_m)(1 + \hat{\sigma}_z)$, with the initial state $(\sqrt{\phi}|\uparrow\rangle + \sqrt{1-\phi}|\downarrow\rangle) \otimes |n_1, n_2, \dots, n_9\rangle$. The Pauli operators ($\hat{\sigma}_{\alpha=x,y,z}$) are associated with the two states $|\uparrow\rangle$ and $|\downarrow\rangle$, representing respectively the presence and absence of a carrier. The bosonic state $|n_1, n_2, \dots, n_9\rangle$ associated with nine vibrational modes is sampled from the Boltzmann distribution $\exp(-\beta \sum_{m=1}^9 \omega_m b_m^\dagger b_m)$. The mean and standard de-

viation (concerning the sampled trajectories) of $\langle \hat{\sigma}_x(t) \rangle$ and $\langle \hat{\sigma}_y(t) \rangle$ ($t \in [0, 100]$ fs) are obtained for each T from a sufficient number of quantum trajectories initiated with the same ϕ [41], but different pure bosonic states. These data are used to optimize a DIQCD model with $\hat{H}_\epsilon^{\text{eff}}(t) = \epsilon_0 \hat{\sigma}_z + \sum_{m=1}^9 \frac{1}{2} \epsilon_m(t) (1 + \hat{\sigma}_z)$ and the jumping operator $(1 + \hat{\sigma}_z)/2$ (γ is the damping rate), for each T separately. Here, ϵ_0 and γ are flexible, time-independent scalars. $\epsilon_m(t)$ is chosen to be a periodic sinusoidal signal with flexible amplitude, fixed frequency ω_m , and random initial phases. These choices are *ad hoc*. But it has been demonstrated in the time-dependent wavepacket diffusion approach [37] that periodic signals serve as a semiclassical approximation to vibrational fluctuation. After training undetermined parameters in $\{\epsilon_0, \gamma\} \cup \{\epsilon_m\}$ with data associated with the time interval $t \in [0, 70]$ fs, DIQCD models yield satisfactory agreement with the data on $\langle \hat{\sigma}_x(t) \rangle$ and $\langle \hat{\sigma}_y(t) \rangle$ (see Fig. 2(b) for the case of $T = 300$ K as an example).

Due to translational symmetry, the one-molecule DIQCD model can be generalized for the molecular lattice as $\hat{H}_\epsilon(t) = \hat{H}_e + \sum_n \sum_{m=1}^9 \epsilon_m^{(n)}(t) c_n^\dagger c_n$ with the jump operator $\hat{L}_n = c_n^\dagger c_n$ (damping rate is γ) on each site. We estimate the carrier mobility by simulating Eq. (1) with the initial condition that one carrier is entirely localized on the middle site of a finite molecular lattice of size $L = 150$ (about $0.1\mu\text{m}$ on length scale). The diffusion of the carrier at $T = 300$ K is illustrated by Fig. 2(d-e), showing a mesoscopic behavior consistent with classical Fick's law. μ is calculated by

$$\mu(T) = \frac{eD^2}{2k_B T} \lim_{t \rightarrow \infty} \frac{d}{dt} \langle \text{Tr}(\rho_\epsilon(t) n^2) - \text{Tr}^2(\rho_\epsilon(t) n) \rangle_\epsilon. \quad (2)$$

As in Ref. [20], we take the intermolecular distance $D = 7\text{\AA}$. μ estimated from DIQCD agree closely with experimental estimation of intrinsic mobility [32], and also the μ calculated from TD-DMRG [20] with the Kubo formula for a system of $L = 21$ sites. The comparisons are shown in Fig. 2(c), which also reports the μ we calculated from the standard Ehrenfest approach [42] (with non-adiabatic force). The Ehrenfest approach deviates significantly from TD-DMRG, because $k_B/\hbar \times 300\text{K} \approx 1300\text{cm}^{-1}$ overlaps with the interval of phonon frequency (hence substantial nuclear quantum effects). However, it is unclear whether the minor but persistent difference between DIQCD and TD-DMRG is due to the finite-size error in TD-DMRG or the approximation made by DIQCD.

Without much modification, the approach reported here can be applied to a two-dimensional lattice model. Point defects can be introduced by training several one-molecule DIQCD models that combine into an inhomogeneous tight-binding Hamiltonian.

Discussion – DIQCD strikes the balance between accuracy and efficiency. In both case studies, DIQCD is trained on data observed on localized one-body or few-body subsystems, reflecting typical scenarios in real-

world data collection. The resultant model is generalized to the whole system by introducing known long-range interactions (dipolar interaction and intermolecular hopping). A strong presumption here is that the noise in long-range interaction is either negligible or can be handled with a known model, which happens to be valid in the two case studies. When such an assumption does not hold, DIQCD should be trained on data observing a larger part of the system. This may require approaches like TD-DMRG or multi-configuration time-dependent Hartree [43] if the data source is numerical simulations.

Although explicit semiclassical approximation has been avoided, we recognize that the application of DIQCD requires a clear phenomenological understanding of the quantum device and what the observables are that govern the dynamical process relevant to device metrics. The challenge is similar to choosing a “good” set of collective variables for describing conformational dynamics of molecules. Although physical intuitions are available for both case studies reported here, for general open quantum systems, one needs a systematic method for defining a canonical transformation that reveals the most relevant low-dimensional observables for data collection.

Data and Code Availability – The Python package QEpsilon is publicly available at Github [24]. A tutorial for using QEpsilon is provided in the online documentation. All results reported in this paper can be reproduced through code examples (“QEpsilon/examples/CaF_qubits” and “QEpsilon/examples/Rubrene_Crystal”) within the package.

Acknowledgement – P.X. thanks Yukai Lu for his tremendous help with the specifications of the CaF qubit experiments and his contributions to preparing the manuscript. P.X. thanks Weitang Li for his help with the specifications of the Holstein model of Rubrene. We thank Zhen Huang and Lin Lin for the fruitful discussion. P.X. was supported by the Alvarez Fellowship of Lawrence Berkeley National Lab under contract No. DE-AC02-05CH11231. K.W. and X.L. were supported by the NSF Grants No. DMS-2111221 and No. CCF-2312456. C.Y. and Y.Z. were supported by the U.S. Department of Energy, Office of Science, Accelerated Research in Quantum Computing Centers, Quantum Utility through Advanced Computational Quantum Algorithms, grant no. DE-SC0025572. A. M. and W.A.dJ. were supported by the U.S. Department of Energy under Contract No. DE-AC02-05CH11231 Office of Science, Accelerated Research in Quantum Computing Centers, FAR-QC. Calculations were performed on the National Energy Research Scientific Computing Center (NERSC), a U.S. Department of Energy Office of Science User Facility operated under Contract No. DE-AC02-05CH11231.

* pinchenxie@lbl.gov

† cyang@lbl.gov

- [1] G. Lindblad, On the generators of quantum dynamical semigroups, *Commun. Math. Phys.* **48**, 119 (1976).
- [2] V. Gorini, A. Kossakowski, and E. C. G. Sudarshan, Completely positive dynamical semigroups of n -level systems, *J. Math. Phys.* **17**, 821 (1976).
- [3] A. Garg, J. N. Onuchic, and V. Ambegaokar, Effect of friction on electron transfer in biomolecules, *J. Chem. Phys.* **83**, 4491 (1985).
- [4] Y. Tanimura and R. Kubo, Time evolution of a quantum system in contact with a nearly gaussian-markoffian noise bath, *J. Phys. Soc. Jpn.* **58**, 101 (1989).
- [5] B. M. Garraway, Decay of an atom coupled strongly to a reservoir, *Phys. Rev. A* **55**, 4636 (1997).
- [6] L. Diósi and W. T. Strunz, The non-markovian stochastic schrödinger equation for open systems, *Phys. Lett. A* **235**, 569 (1997).
- [7] Y. Tanimura, Stochastic liouville, langevin, fokker-planck, and master equation approaches to quantum dissipative systems, *J. Phys. Soc. Jpn.* **75**, 082001 (2006).
- [8] R.-X. Xu and Y. Yan, Dynamics of quantum dissipation systems interacting with bosonic canonical bath: Hierarchical equations of motion approach, *Phys. Rev. E* **75**, 031107 (2007).
- [9] D. Suess, A. Eisfeld, and W. Strunz, Hierarchy of stochastic pure states for open quantum system dynamics, *Phys. Rev. Lett.* **113**, 150403 (2014).
- [10] D. Tamascelli, A. Smirne, S. F. Huelga, and M. B. Plenio, Nonperturbative treatment of non-markovian dynamics of open quantum systems, *Phys. Rev. Lett.* **120**, 030402 (2018).
- [11] K. Wang and X. Li, Simulation-assisted learning of open quantum systems, *Quantum* **8**, 1407 (2024).
- [12] X. Li, Markovian embedding procedures for non-markovian stochastic schrödinger equations, *Phys. Lett. A* **387**, 127036 (2021).
- [13] G. Park, Z. Huang, Y. Zhu, C. Yang, G. K.-L. Chan, and L. Lin, Quasi-lindblad pseudomode theory for open quantum systems, *Phys. Rev. B* **110**, 195148 (2024).
- [14] Z. Huang, G. Park, G. K. Chan, and L. Lin, Coupled lindblad pseudomode theory for simulating open quantum systems, *arXiv preprint arXiv:2506.10308* (2025).
- [15] P. Ehrenfest, Bemerkung über die angenäherte gültigkeit der klassischen mechanik innerhalb der quantenmechanik, *Z. Phys.* **45**, 455 (1927).
- [16] J. C. Tully, Molecular dynamics with electronic transitions, *J. Chem. Phys.* **93**, 1061 (1990).
- [17] J. E. Subotnik, A. Jain, B. Landry, A. Petit, W. Ouyang, and N. Bellonzi, Understanding the surface hopping view of electronic transitions and decoherence, *Annu. Rev. Phys. Chem.* **67**, 387 (2016).
- [18] A. L. Shaw, *Learning, Verifying, and Erasing Errors on a Chaotic and Highly Entangled Programmable Quantum Simulator*, Ph.D. thesis, California Institute of Technology (2024).
- [19] C. M. Holland, Y. Lu, and L. W. Cheuk, On-demand entanglement of molecules in a reconfigurable optical tweezer array, *Science* **382**, 1143 (2023).
- [20] W. Li, J. Ren, and Z. Shuai, Finite-temperature TD-DMRG for the carrier mobility of organic semiconductors, *J. Phys. Chem. Lett.* **11**, 4930 (2020).
- [21] Y. Cao and J. Lu, Structure-preserving numerical schemes for lindblad equations, *J. Sci. Comput.* **102**, 27 (2025).
- [22] Z. Zhang, X. Liu, K. Yan, M. E. Tuckerman, and J. Liu, Unified efficient thermostat scheme for the canonical ensemble with holonomic or isokinetic constraints via molecular dynamics, *J. Phys. Chem. A* **123**, 6056 (2019).
- [23] Such as the damping time in a Langevin process and the angular frequency of an harmonic oscillator.
- [24] QEpsilon, <https://github.com/salinelake/QEpsilon>, accessed: 2025-08-22.
- [25] A. M. Kaufman and K.-K. Ni, Quantum science with optical tweezer arrays of ultracold atoms and molecules, *Nat. Phys.* **17**, 1324 (2021).
- [26] S. Burchesky, L. Anderegg, Y. Bao, S. S. Yu, E. Chae, W. Ketterle, K.-K. Ni, and J. M. Doyle, Rotational coherence times of polar molecules in optical tweezers, *Phys. Rev. Lett.* **127**, 123202 (2021).
- [27] Y. Bao, S. S. Yu, L. Anderegg, E. Chae, W. Ketterle, K.-K. Ni, and J. M. Doyle, Dipolar spin-exchange and entanglement between molecules in an optical tweezer array, *Science* **382**, 1138 (2023).
- [28] Y. Lu, S. J. Li, C. M. Holland, and L. W. Cheuk, Raman sideband cooling of molecules in an optical tweezer array, *Nat. Phys.* **20**, 389 (2024).
- [29] The word “flexible” indicates quantities that will be optimized with data.
- [30] The qubit loss is severe for $d < 1.68\mu\text{m}$ due to parametric heating of molecules. For the same reason, the current DIQCD model with a fixed molecular temperature can not be directly applied to $d < 1.68\mu\text{m}$.
- [31] D. Marx and M. Parrinello, Ab initio path integral molecular dynamics: Basic ideas, *J. Chem. Phys.* **104**, 4077 (1996).
- [32] J. Takeya, M. Yamagishi, Y. Tominari, R. Hirahara, Y. Nakazawa, T. Nishikawa, T. Kawase, T. Shimoda, and S. Ogawa, Very high-mobility organic single-crystal transistors with in-crystal conduction channels, *Appl. Phys. Lett.* **90** (2007).
- [33] J. Mei, Y. Diao, A. L. Appleton, L. Fang, and Z. Bao, Integrated materials design of organic semiconductors for field-effect transistors, *J. Am. Chem. Soc.* **135**, 6724 (2013).
- [34] X. Ren, M. J. Bruzek, D. A. Hanifi, A. Schulzetenberg, Y. Wu, C.-H. Kim, Z. Zhang, J. E. Johns, A. Salleo, S. Fratini, *et al.*, Negative isotope effect on field-effect hole transport in fully substituted 13c-rubrene, *Adv. Electron. Mater.* **3**, 1700018 (2017).
- [35] This happens to be the case for most high-mobility organic semiconductors.
- [36] The success of TD-DMRG is also limited to 1D due to the 1D nature of the matrix product state and the numerical inefficiency of higher-dimensional tensor networks.
- [37] Y. Jiang, X. Zhong, W. Shi, Q. Peng, H. Geng, Y. Zhao, and Z. Shuai, Nuclear quantum tunnelling and carrier delocalization effects to bridge the gap between hopping and bandlike behaviors in organic semiconductors, *Nanoscale Horiz.* **1**, 53 (2016).
- [38] A. D. Becke, Density-functional thermochemistry. iii. the role of exact exchange, *J. Chem. Phys.* **98**, 5648 (1993).
- [39] C. Lee, W. Yang, and R. G. Parr, Development of the colle-salvetti correlation-energy formula into a functional of the electron density, *Phys. Rev. B* **37**, 785 (1988).

- [40] M. J. Frisch and *et al.*, *Gaussian 09 Revision D.01 ed.*, Gaussian Inc., Wallingford, CT (2009).
- [41] Results are not sensitive to the choice of ϕ .
- [42] L. Wang, D. Beljonne, L. Chen, and Q. Shi, Mixed quantum-classical simulations of charge transport in organic materials: Numerical benchmark of the suschrieffer-heeger model, *J. Chem. Phys* **134** (2011).
- [43] H.-D. Meyer, U. Manthe, and L. S. Cederbaum, The multi-configurational time-dependent hartree approach, *Chem. Phys. Lett.* **165**, 73 (1990).

APPENDIX

Appendix A - QEpsilon

A schematic representation of the structure of QEpsilon is shown in Fig. 3. QEpsilon can be roughly divided into the following modules: (1) a library of second-quantized bosonic, spin, and tight-binding operators as the basis for composing a many-body Hamiltonian and the jump operators; (2) a library of typical classical-process integrators and structure-preserving quantum integrators (we adopt the $M = 1$ integrator in Ref. [21] for Lindblad equation) for parameterizing $\epsilon(t)$; (3) a user interface for composing a many-body mixed system with these libraries; (4) several structure-preserving quantum integrators for simulating unitary and Lindblad dynamics; (5) a mechanism to train $\epsilon(t)$ on time-series data with backpropagation. These modularized components allow training and large-scale simulation in a unified, GPU-enabled framework. More technical details of QEpsilon should be found in the online documentation of the open-source package [24].

Appendix B: CaF molecular qubits

Optical Tweezer – A single optical tweezer has a Gaussian trapping potential $U_T(r, z) = -V \left(\frac{w_0}{w(z)} \right)^2 e^{-\frac{2r^2}{w^2(z)}}$ with respect to radial distance r and height z from the center. $V_m = k_B \times 1.28\text{mK}$ is the maximal depth of the trap. $w_0 = 730\text{nm}$ is the waist of the beam while $w(z) = w_0 \sqrt{1 + (z/z_R)^2}$ with the Rayleigh range $z_R = \pi w_0^2/\lambda$. $\lambda = 781\text{nm}$ is the wavelength. When performing a two-qubit gate, the central depth of the trap is limited to $V \approx k_B \times 0.13\text{mK}$.

XY8 sequence – The size of each XY8 block (see Fig. 1) is 1.6ms for one-qubit experiments and two-qubit experiments with $d < 1.68\mu\text{m}$, 3.2ms for two-qubit experiments with $d \geq 1.68\mu\text{m}$.

CaF molecules – The coupling constant for dipole-dipole interaction is $J_0 = 1942.3\hbar \cdot \text{Hz} \cdot \mu\text{m}^3$ [19]. When performing the two-qubit gate, Raman thermometry gives a rough estimation of the molecular temperature that amounts to $T_r = 6\mu\text{K}$ for radial motion (parallel to xy plane) and $T_a = 18\mu\text{K}$ for axial motion (z direction). Note that the molecular temperature changes with the depth of the optical trap. So the molecular temperature here is much lower than the temperature estimated at full depth [19].

Bell State creation – The scheme is illustrated by Fig. 1(b). The initial state is $|\uparrow\uparrow\rangle$. Two $\pi/2$ pulses along the x axis are applied at the start and the end of the scheme. XY8 sequences are applied consecutively for error suppression.

Molecular dynamics of $R(t)$ – Standard Langevin integrator [22] is used to simulate the molecular dynamics of $R(t)$. The radial (x and y directions) and axial (z direction) motion are controlled with the same friction constant (damping time $\tau = 100\text{ms}$) but different amplitude

m	1	2	3	4	5	6	7	8	9
ω_m/cm^{-1}	84	214	632	1002	1206	1351	1364	1535	1594
g_m	0.96	0.37	0.25	0.20	0.15	0.31	0.13	0.20	0.31

TABLE I. Frequency of kept vibrational modes and the renormalized coupling constants.

of white noise to maintain their respective temperature $T_r = 6\mu\text{K}$ and $T_a = 18\mu\text{K}$.

Training – We train the DIQCD model with all twenty-four one-qubit data (see Fig. 1) simultaneously. For each epoch, we simulate DIQCD three times, respectively with plain, spin-echo, and XY8 control schemes. The batch size for each simulation is 512. The time step for integration is 0.01ms for the plain scheme, 0.05ms for the spin-echo scheme, and 0.1ms for the XY8 scheme. The loss function is $L = \frac{1}{7} \sum_{i=1}^7 (C_i^{\text{M,Plain}} - \varsigma^{-1} C_i^{\text{D,Plain}})^2 + \frac{1}{10} \sum_{i=1}^{10} (C_i^{\text{M,Echo}} - \varsigma^{-1} C_i^{\text{D,Echo}})^2 + \frac{1}{7} \sum_{i=1}^7 (C_i^{\text{M,XY8}} - \varsigma^{-1} C_i^{\text{D,XY8}})^2$. The superscript “M” and “D” indicate the Model and the Data, respectively. $C_i^{\text{D,Plain}}$ is the i -th ($i = 1, 2, \dots, 7$) data point associated with the plain scheme. $C_i^{\text{M,Plain}}$ is the corresponding DIQCD model prediction. The meaning of $C_i^{\text{M,Echo}}$, $C_i^{\text{D,Echo}}$, $C_i^{\text{M,XY8}}$, $C_i^{\text{D,XY8}}$ are self-evident. The DIQCD model is trained for 200 epochs, with the standard ADAM optimizer in PyTorch with a fixed learning rate of 0.1 for all parameters but the damping rates γ_x and γ_z . The learning rate for damping rates is set to 0.001. The loss saturates after roughly 50 epochs. The final productive DIQCD model is chosen to be the model trained after all the epochs. The training is done with QEpsilon and a CPU node on Perlmutter. Training with a GPU is not necessary for a small quantum system.

Appendix C: Rubrene Crystal

Electron-phonon coupling – Parameters for electron-phonon coupling in Rubrene were derived in Ref. [20, 37] from density functional theory calculations with B3LYP functional approximation [38], the 6-31G(d) basis set, and the Gaussian 09 software [40]. Each Rubrene molecule has 210 vibrational modes, with tens of them contributing to electron-phonon coupling. To reduce the complexity of the effective Hamiltonian describing electron-phonon interaction, one can keep only a few modes with significant electron-phonon coupling and renormalize their coupling constants to conserve the total reorganization energy. The effective model adopted here keeps nine modes, with frequency (ω_m) and coupling constant (g_m) listed in Table I.

Data generation – We generate our data by simulating the plain unitary quantum dynamics with a timestep of 0.01fs. We use $\phi = 0.1$ throughout the work. The total sample time for each unitary simulation is 100fs. For

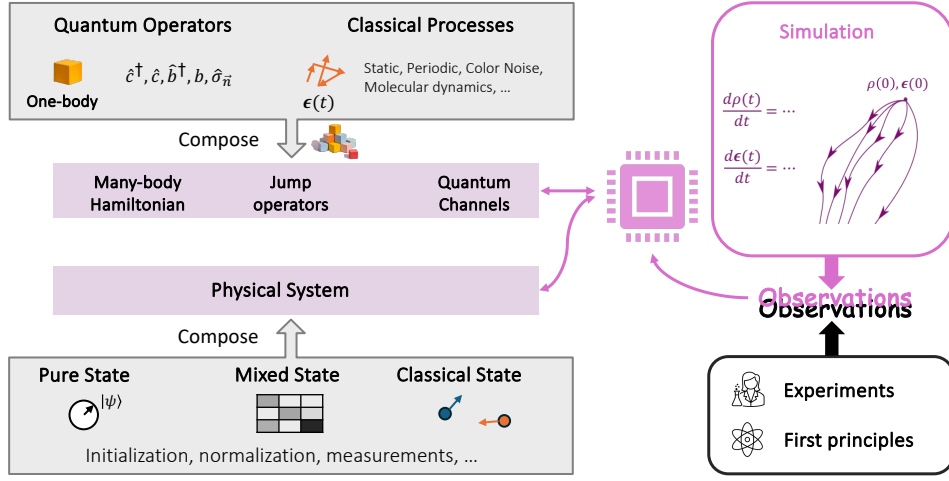
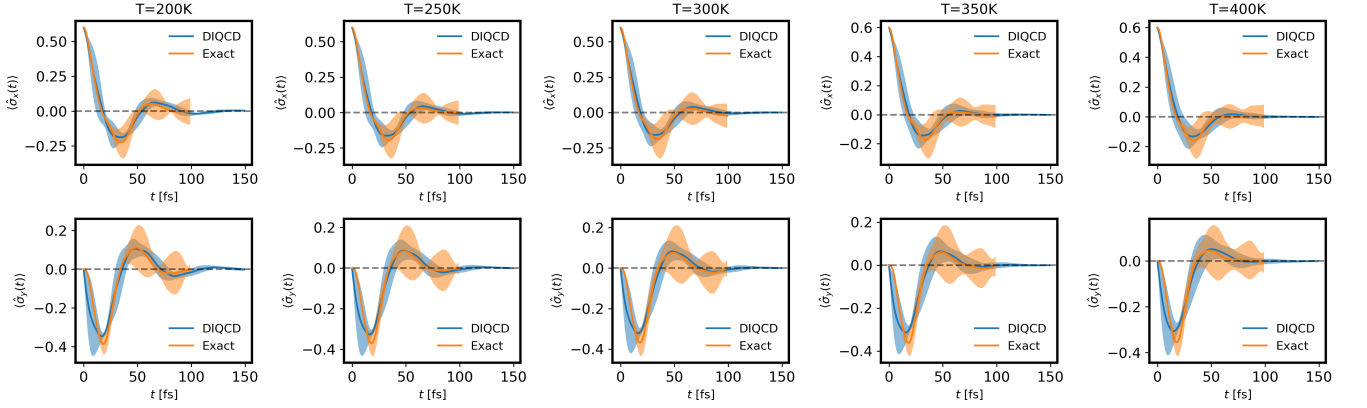


FIG. 3. The structure of QEpsilon.

FIG. 4. The mean and standard deviation (concerning the ensemble of sampled trajectories) of $\langle \hat{\sigma}_x(t) \rangle$ and $\langle \hat{\sigma}_y(t) \rangle$ from the final DIQCD models and the data associated with exact unitary simulation.

each temperature ($T=200\text{K}, 250\text{K}, 300\text{K}, 350\text{K}, 400\text{K}$) separately, we generate 64 trajectories of unitary evolution. Then, we calculate the mean and standard deviation on observing $\hat{\sigma}_x(t)$ and $\hat{\sigma}_y(t)$ at $t = 0, 1, 2, \dots, 99\text{fs}$. The simulation is done with QEpsilon and one NVIDIA A100 GPU.

Training – For each temperature separately, we train a DIQCD model with a subset of one-molecule data associated with the sampling time interval $t \in [0, 70]\text{fs}$. The loss function is $L = \sum_{i=1}^{70} (\text{Mean}^M[\hat{\sigma}_x(i \cdot \text{fs})] - \text{Mean}^D[\hat{\sigma}_x(i \cdot \text{fs})])^2 + (\text{Mean}^M[\hat{\sigma}_y(i \cdot \text{fs})] - \text{Mean}^D[\hat{\sigma}_y(i \cdot \text{fs})])^2 + 0.1(\text{STD}^M[\hat{\sigma}_x(i \cdot \text{fs})] - \text{STD}^D[\hat{\sigma}_x(i \cdot \text{fs})])^2 + 0.1(\text{STD}^M[\hat{\sigma}_y(i \cdot \text{fs})] - \text{STD}^D[\hat{\sigma}_y(i \cdot \text{fs})])^2$. The superscript “M” and “D” indicate the Model and the Data, respectively. “MEAN” and “STD” represent mean value and standard deviation

concerning the 64 trajectories. Note that the loss concerning standard deviation weights 0.1 due to its minor regularization role. The forward evolution of DIQCD uses a batch size of 512 and a timestep of 0.05fs. Each DIQCD model is trained for 200 epochs of forward evolution, with the standard ADAM optimizer in PyTorch with a fixed learning rate of 0.3. Model parameters converge after roughly 150 epochs. The final productive DIQCD model is chosen to be the model trained after all the epochs. The training is done with QEpsilon and one NVIDIA A100 GPU. A comparison between the final DIQCD models and the data is provided in Fig. 4.

Simulation – Simulation of the DIQCD models for a molecular lattice of size $L = 150$ is done with QEpsilon and one NVIDIA A100 GPU. The batch size for forward evolution is 512, and the timestep is 0.01fs. The total sample time is 100fs for calculating the carrier mobility.